Supplementary Materials for

Structure-based design of prefusion-stabilized SARS-CoV-2 spikes

Ching-Lin Hsieh, Jory A. Goldsmith, Jeffrey M. Schaub, Andrea M. DiVenere, Hung-Che Kuo, Kamyab Javanmardi, Kevin C. Le, Daniel Wrapp, Alison G. Lee, Yutong Liu, Chia-Wei Chou, Patrick O. Byrne, Christy K. Hjorth, Nicole V. Johnson, John Ludes-Meyers, Annalee W. Nguyen, Juyeon Park, Nianshuang Wang, Dzifa Amengor, Jason J. Lavinder, Gregory C. Ippolito, Jennifer A. Maynard*, Ilya J. Finkelstein*, Jason S. McLellan*

*Corresponding author. Email: maynard@che.utexas.edu (J.A.M.); ilya@finkelsteinlab.org (I.J.F.); jmclellan@austin.utexas.edu (J.S.M.)

This PDF file includes:

Materials and Methods
Figs. S1 to S6
Tables S1 to S3
References

Materials and Methods

Design scheme for prefusion-stabilized SARS-CoV-2 spike variants

The SARS-CoV-2 S-2P variant was used as the base construct for all subsequent designs (*18*).

The S-2P base construct comprises residues 1-1208 of SARS-CoV-2 S (GenBank: MN908947)

with prolines substituted at residues 986 and 987, "GSAS" substituted at the furin cleavage site

(residues 682–685), and C-terminal foldon trimerization motif, HRV3C protease recognition site,

Twin-Strep-tag and octa-histidine tag cloned into the mammalian expression plasmid pαH. Using

this plasmid as a template, desired mutations were introduced at selected positions within the

SARS-CoV-2 S2 subunit. Based on SARS-CoV-2 S-2P cryo-EM structure (PDB ID: 6VSB),

pairs of residues with Cβ atoms less than 4.6 Å apart were considered for disulfide bond designs.

We particularly targeted the regions that move drastically during the pre- to postfusion transition

such as the fusion peptide, connector region and HR1. Salt bridge variants required that the

charged groups of the substituted residues were predicted to be within 4.0 Å. For residues in

loops, a slightly longer distance than 4.0 Å was allowed. Core-facing residues with sidechains

adjacent to a pre-existing internal cavity were examined for potential substitutions to bulkier

hydrophobic residues. Proline substitutions were designed in the FP, connector region, or HR1

and placed either in a flexible loop or at the N-terminus of a helix. Combinations were chosen to

test whether pairs of the same type of design (e.g. disulfide/disulfide) or different types of

designs (e.g. disulfide/proline) could result in additive effects on spike expression and stability.

Protein expression and purification

Plasmids encoding S variants were transiently transfected into FreeStyle 293-F cells (Thermo

Fisher) using polyethyleneimine, with 5 μM kifunensine being added 3h post-transfection.

Cultures were harvested four days after transfection and the medium was separated from the cells

by centrifugation. Supernatants were passed through a 0.22 µm filter and then over StrepTactin resin (IBA). Spike variants were further purified by size-exclusion chromatography using a Superose 6 10/300 column (GE Healthcare) in a buffer composed of 2 mM Tris pH 8.0, 200 mM NaCl and 0.02% NaN_3. For initial purification and characterization, single-substitution and combination spike variants were purified from 40 mL cultures. For the 1L HexaPro purification, the size-exclusion column used was a Superose 6 16/600 column (GE Healthcare).

ExpiCHO cells were transiently transfected with a plasmid encoding HexaPro using Expifectamine, and cells were grown for six days at 32 °C according to the manufacturer's High Titer protocol (Thermo Fisher). Supernatants were then passed through a 0.22 µm filter, flowed over Strep-Tactin resin, and subsequently purified by size-exclusion chromatography using a Superose 6 10/300 column (GE Healthcare) in a buffer composed of 2 mM Tris pH 8.0, 200 mM NaCl and 0.02% NaN_3.

Differential scanning fluorimetry

In a 96-well qPCR plate, solutions were prepared with a final concentration of 5X SYPRO Orange Protein Gel Stain (Thermo Fisher) and 0.25 mg/mL spike. Continuous fluorescence measurements (λ_{ex}=465 nm, λ_{em}=580 nm) were performed using a Roche LightCycler 480 II, using a temperature ramp rate of 4.4 °C/minute increasing from 22 °C to 95 °C. Data were plotted as the derivative of the melting curve as a function of temperature.

Negative stain EM

Purified SARS-CoV-2 S variants were diluted to a concentration of 0.04 mg/mL in 2 mM Tris pH 8.0, 200 mM NaCl and 0.02% NaN_3. Each protein was deposited on a CF-400-CU grid (Electron Microscopy Sciences) that had been plasma cleaned for 30 seconds in a Solarus 950 plasma cleaner (Gatan) with a 4:1 ratio of O_2/H_2 and stained using methylamine tungstate

(Nanoprobes). Grids were imaged at a magnification of 92,000X (corresponding to a calibrated

pixel size of 1.63 Å/pix) in a Talos F200C TEM microscope equipped with a Ceta 16M detector

(Thermo Fisher). Stability experiments with S-2P and HexaPro were performed by imaging

samples as described above after 3 rounds of snap freezing with liquid nitrogen and thawing,

after storing samples at room temperature for 1-2 days, or after incubating at 50 °C, 55 °C, or 60

°C for 30 minutes in a thermal cycler.

Biolayer interferometry for quantification of protein expression

Plasmids encoding spike variants were transfected into FreeStyle 293-F cells (Thermo Fisher) in

3 mL of medium and harvested four days after transfection. After centrifugation, supernatant was

diluted 5-fold with buffer composed of 10 mM HEPES pH 7.5, 150 mM NaCl, 3 mM EDTA,

0.05% Tween 20 and 1 mg/mL bovine serum albumin. Anti-foldon IgG was immobilized to an

anti-human Fc (AHC) biosensor (FortéBio) using an Octet RED96e (FortéBio). The IgG loaded

biosensor was then dipped into wells containing individual spike variants. A standard curve was

determined by measuring 2-fold serial dilutions of purified S-2P at concentrations ranging from

10 μg/mL to 0.16 μg/mL. The data were reference-subtracted, aligned to a baseline after IgG

capture and quantified based on a linear fit of the initial slope for each association curve using

Octet Data Analysis software v11.1. Transfections and subsequent measurements of spike

concentration were carried out in triplicate.

ELISA

To examine the antigenicity of spike variants, S-2P and HexaPro were coated on a Costar® 96-

well assay plates (High Binding polystyrene, Corning) overnight at 4°C. After blocking with 2%

milk for 2 hours, serial dilutions of the positive sera, mAb CR3022, or negative serum control

(GNEG) were added and incubated for 1 hour at room temperature. After three washes with

PBS-T, anti-human IgG Fab HRP (Sigma cat # A0293) (1:5000 dilution) was added to the plate

for 30 minutes. Finally, 1-step Ultra TMB ELISA substrate (Thermo Fisher) was applied to

develop the colorimetric signal. The reactions were stopped by H_2SO_4 and absorbance was read

on a microplate reader at 450 nm.

Human sera

Plasma from K2-EDTA anti-coagulated whole blood specimens was acquired from two

recovered COVID-19 patients (approximately 50 days post-onset of symptoms) who had tested

positive for SARS-CoV-2 by RT-PCR assay during acute-phase infection. Donors provided

informed consent for blood collection which was performed using standard techniques approved

by the University of Texas at Austin institutional review board (protocol number 2020-03-0085).

Surface plasmon resonance

His-tagged HexaPro was immobilized to a NiNTA sensorchip (GE Healthcare) to a level of ~500

response units (RUs) using a Biacore X100 (GE Healthcare) and running buffer composed of 10

mM HEPES pH 8.0, 150 mM NaCl and 0.05% Tween 20. Serial dilutions of purified hACE2

were injected at concentrations ranging from 250 to 15.6 nM. Response curves were fit to a 1:1

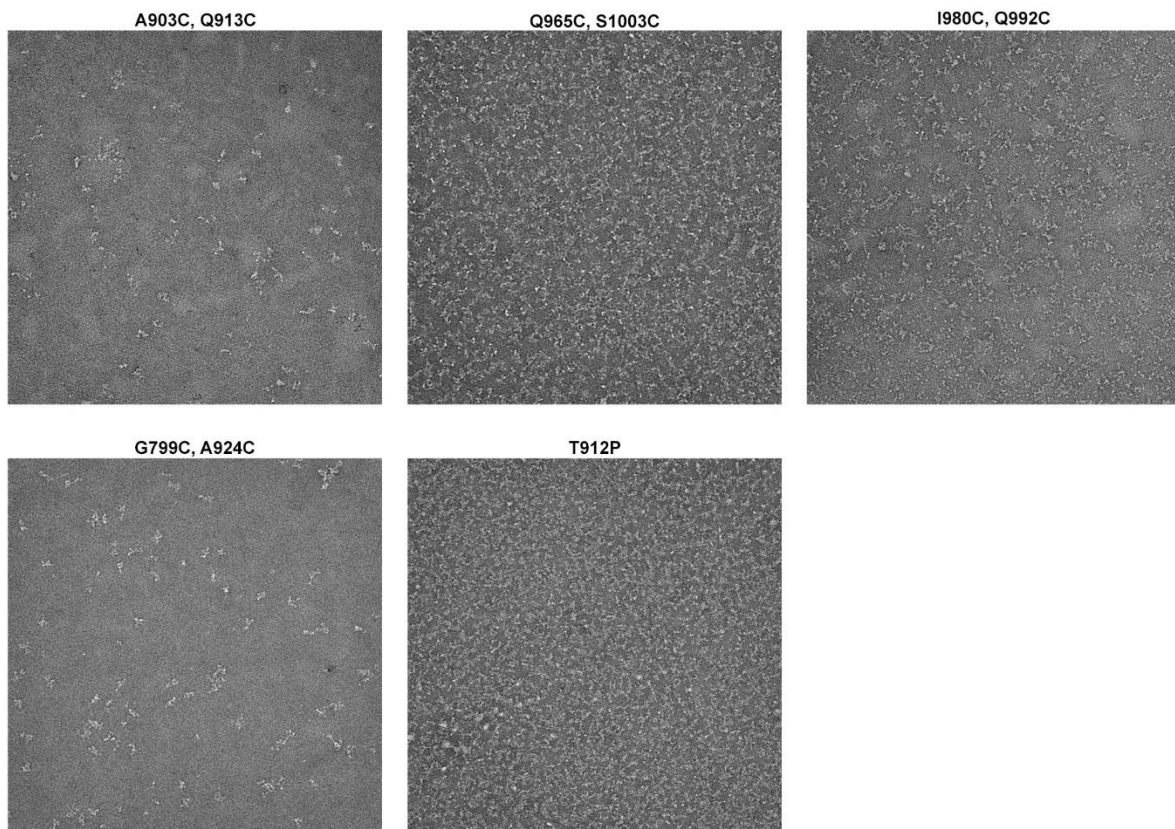binding model using Biacore X100 Evaluation Software (GE Healthcare).

Cryo-EM sample preparation and data collection

Purified HexaPro was diluted to a concentration of 0.35 mg/mL in 2 mM Tris pH 8.0, 200 mM

NaCl, 0.02% NaN_3 and applied to plasma-cleaned CF-400 1.2/1.3 grids before being blotted for

6 seconds in a Vitrobot Mark IV (Thermo Fisher) and plunge frozen into liquid ethane. 3,511

micrographs were collected from a single grid using a FEI Titan Krios (Thermo Fisher) equipped

with a K3 detector (Gatan). Data were collected at a magnification of 81,000x, corresponding to
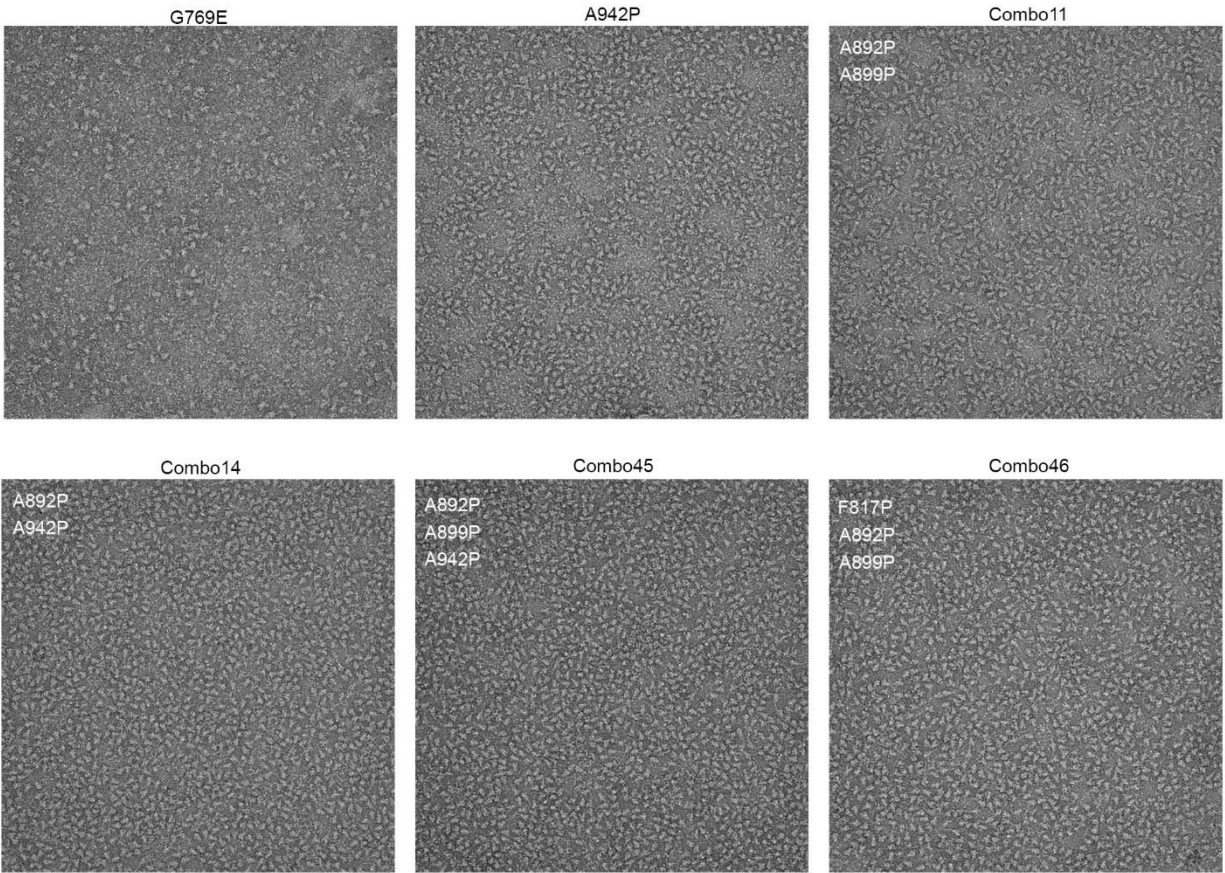
a calibrated pixel size of 1.08 Å/pix. A full description of the data collection parameters can be found in **Table S3**.

Cryo-EM data processing

Motion correction, CTF-estimation and particle picking were performed in Warp (*28*). Particles were then imported into cryoSPARC v2.15.0 for 2D classification, *ab initio* 3D reconstruction, heterogeneous 3D refinement and non-uniform homogeneous refinement (*29*). The one-RBD-up reconstruction was subjected to local B-factor sharpening using LocalDeBlur (*30*) and the two-RBD-up reconstruction was sharpened in cryoSPARC. Iterative model building and refinement were performed with Coot, Phenix and ISOLDE (*31–33*).

A903C, Q913C

Q965C, S1003C

I980C, Q992C

G799C, A924C

T912P

Figure S1. Negative-stain EM images of variants with left-shifted SEC peaks.

G769E

A942P

Combo11

A892P
A899P

Combo14

A892P
A942P

Combo45

A892P
A899P
A942P

Combo46

F817P
A892P
A899P

Figure S2. Negative-stain EM images of well-folded particles.
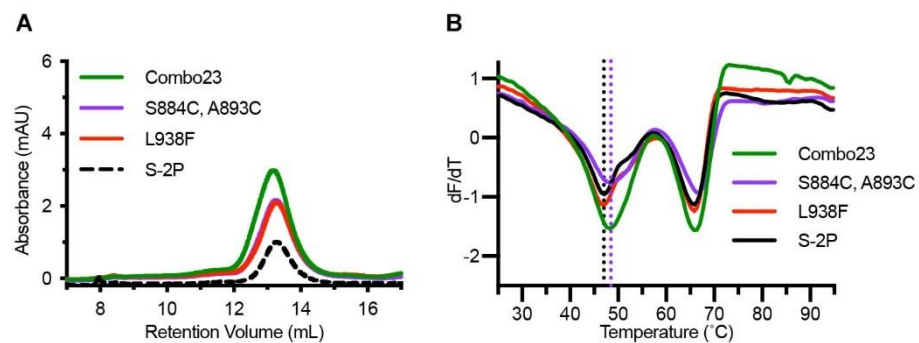
**Figure S3. Characterization of a disulfide and cavity-filling combination variant**

(Combo23). (A) SEC traces of S-2P, Combo23, and the parental variants S884C/A893C

(disulfide bond) and L938F (cavity filling). (B) DSF melting temperature analysis of S-2P,

Combo23, and its parental variants. The black dashed line represents the Tm of S-2P, and the

purple dashed line represents the Tm of S884C/A893C.
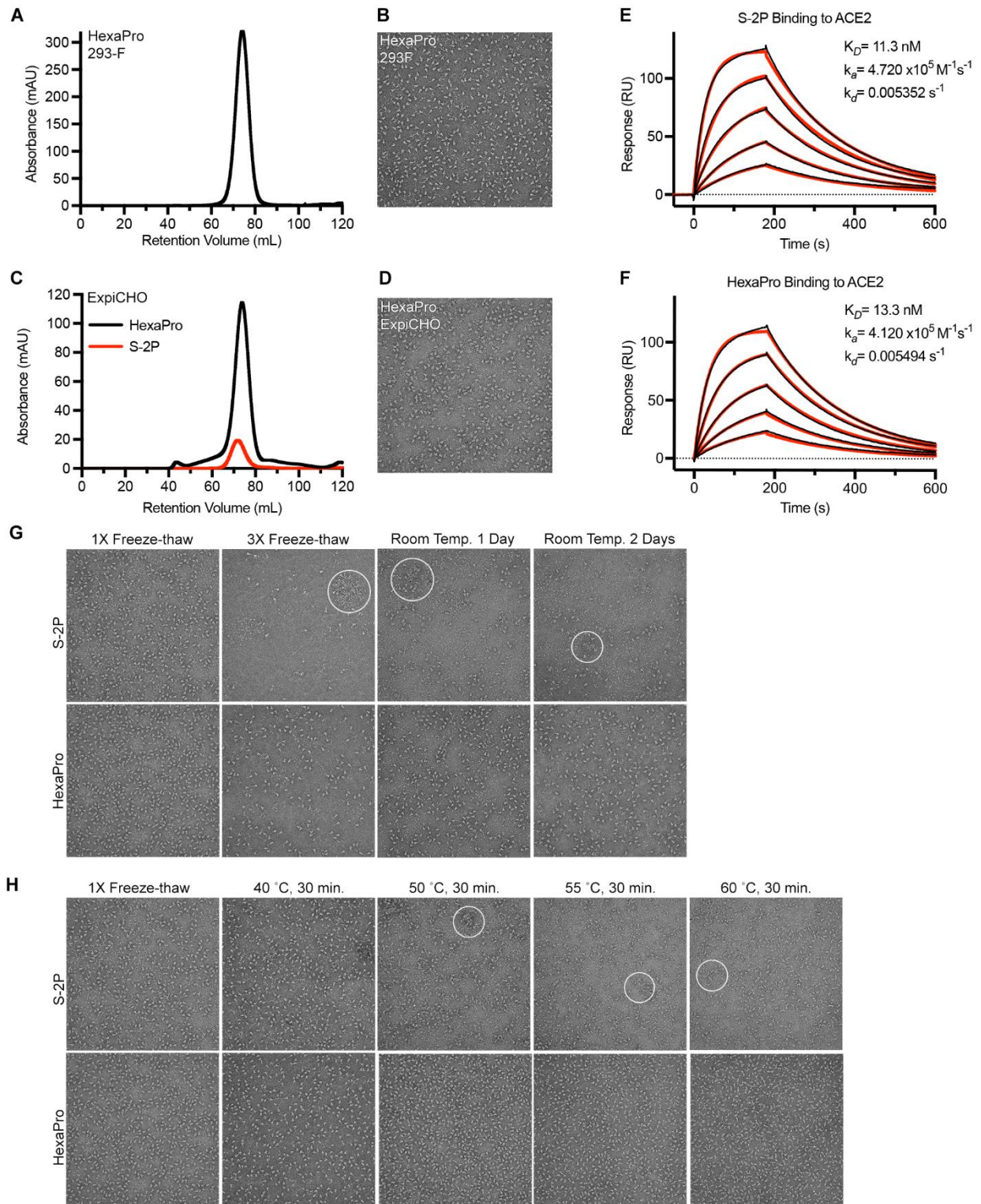
Figure S4. HexaPro exhibits enhanced expression and stability compared to S-2P. (A) SEC

trace of HexaPro purified from a 1L culture of FreeStyle 293-F cells. (B) Negative stain electron

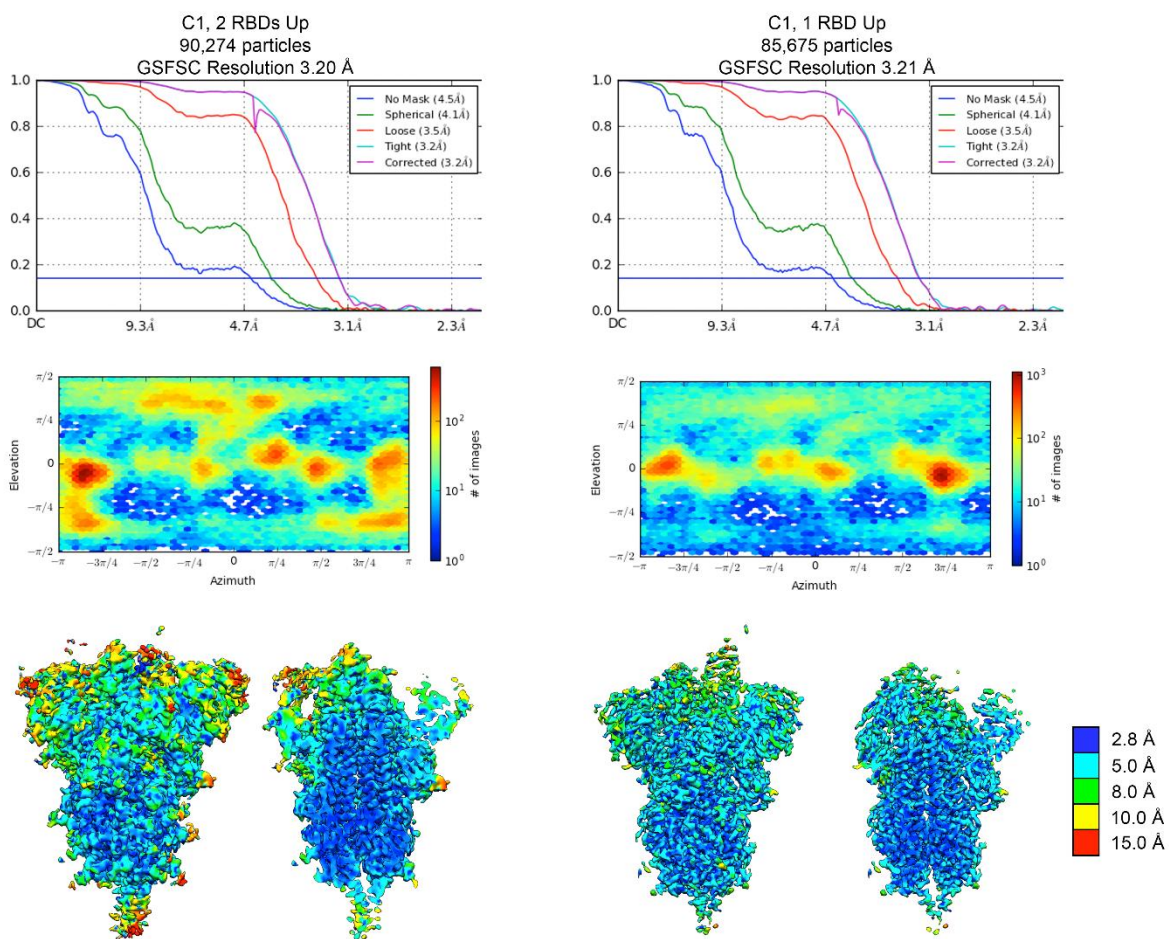micrograph of HexaPro purified from FreeStyle 293-F cells. (C) SEC traces of S-2P and HexaPro purified from ExpiCHO cells. (D) Negative stain electron micrograph of HexaPro from ExpiCHO cells. (E-F) Binding of S-2P (E) and HexaPro (F) to human ACE2 assessed by surface plasmon resonance. Binding data are shown as black lines and the best fit to a 1:1 binding model is shown as red lines. (G-H) Assessment of protein stability by negative stain electron microscopy. The top row of micrographs in (G) and (H) corresponds to S-2P, the bottom row corresponds to HexaPro. Representative debris/aggregates are shown in circles.

Motion Correction
Defocus Estimation
Particle Picking
(Warp)

2D Classification
(cryoSPARC v2)

695,490 particles

409,232 particles

Ab initio
Reconstruction
(cryoSPARC v2)

Heterogeneous
Refinement
(cryoSPARC v2)

Ab initio and Heterogeneous
Refinement
(cryoSPARC v2)

Ab initio and Heterogeneous
Refinement
(cryoSPARC v2)

Non-Uniform
Refinement
(cryoSPARC v2)

1 RBD up
3.21 Å
85,675 particles

2 RBDs up
3.20 Å
90,274 particles

Figure S5. Cryo-EM data processing workflow.

Figure S6. Cryo-EM structure validation. FSC curves and viewing distribution plots, generated in cryoSPARC v2.15, are shown for both the two-RBD-up (*left*) and the one-RBD-up (*right*) reconstruction. Cryo-EM density of each reconstruction is shown and colored according to local resolution, with a central slice through the density shown to the right.

Table S1. Expression summary of variants with single substitutions.

Substitution(s)	Strategy	Fold change in expression relative to S-2P
T547C, N978C	Disulfide	0[b]
A570C, V963C	Disulfide	0[b]
S659C, S698C	Disulfide	0.4[a]
Replace (673-686) with GS	Remove flexible region	0[b]
Replace (673-686) with GS + A672C, A694C	Disulfide, Remove flexible region	<0.5[b]
N703Q, V705C, A893C	Disulfide	<0.5[b]
V705C, A893C	Disulfide	<0.5[b]
A713S	H bond	1.0[a]
V722C, A930C	Disulfide	<0.1[b]
T724M	Cavity-filling	1.3[a]
L727C, S1021C	Disulfide	<0.5[b]
P728C, V951C	Disulfide	0[b]
V729C, A1022C	Disulfide	<0.1[a]
S730L	Cavity-filling	0[b]
S730R	Salt bridge	0.15[a]
S735C, T859C	Disulfide	<0.5[b]
V736C, L858C	Disulfide	0[b]
T752K	Salt bridge	<0.5[b]
A766E	Salt bridge	<0.5[b]
G769E	Salt bridge	3.0[a]
I770C, A1015C	Disulfide	<0.5[b]
T778Q	Hydrogen bond	2.6[a]
T778L	Cavity-filling	1.5[a]
T791C, A879C	Disulfide	1.0[b]
G799C, A924C	Disulfide	1.3[a]
P807C, S875C	Disulfide	1.1[a]
F817P	Proline	2.8[a]
E819C, S1055C	Disulfide	0[b]
E819C, Q1054C	Disulfide	0[b]
L822C, A1056C	Disulfide	0[b]
V826L	Cavity-filling	1.0[b]
L828K	Salt bridge	0.8[a]
L828R	Salt bridge	0.4[a]
Δ(829-851)	Remove flexible region	<0.5[b]
T859K	Salt bridge	2.1[a]
P862E	Salt bridge	<0.5[b]
L865P, Q779M	Proline, cavity-filling	<0.5[b]
T866P	Proline	<0.5[b]
I870C, S1055C	Disulfide	0[b]
T874C, S1055C	Disulfide	<0.5[b]
S875F	Cavity-filling	<0.5[b]
S884C, A893C	Disulfide	1.5[a]
G885C, Q901C	Disulfide	1.1[a]
G889C, L1034C	Disulfide	<0.1[a]
A890V	Cavity-filling	1.0[b]
A892P	Proline, cavity-filling	1.4[a]
A893P	Proline	1.5[b]
L894F	Cavity-filling	0.9[a]
Q895P	Proline	2.1[b]
I896C, Q901C	Disulfide	0[b]
A899F	Cavity-filling	0.3[b]
A899P	Proline, Cav	1.2[a]
Q901M	Cavity-filling	0.9[a]
A903C, Q913C	Disulfide	0.82[b]
V911C, N1108C	Disulfide	0[b]
T912R	Salt bridge	<0.5[b]
T912P	Proline cavity-filling	1.5[a]
K921P	Proline	1.1[b]
L922P	Proline	0.8[b]
L938F	Cavity-filling	2.0[a]
A942P	Proline	6.0[a]
A944F	Cavity-filling	1.0[a]
A944F, T724I	Cavity-filling	0.4[a]
A944Y	Cavity-filling	1.9[b]
G946P	Proline	1.0[b]
Q957E	Salt bridge	1.0[a]
T961D	Salt bridge	1.8[a]
T961C, S758C	Disulfide	0[b]
T961C, Q762C	Disulfide	0[b]
V963L	Cavity-filling	1.8[a]
Q965C, S1003C	Disulfide	3.8[a]
A972C, Q992C	Disulfide	1[a]
A972C, I980C	Disulfide	1.3[a]
S974C, D979C	Disulfide	0.3[b]
S975P	Proline	2.2[b]
N978P	Proline	0.9[b]

14

I980C, Q992C	Disulfide	2.0[a]
R1000Y	Cavity-filling + hydrogen bond	0.3[a]
R1000W	Cavity-filling	1.0[a]
S1003V	Cavity-filling	1.9[b]
I1013F	Cavity-filling	0.8[a]
R1039F	Charge removal, pi-pi stacking	0.5[b]
V1040F	Cavity-filling	<0.5[b]
V1040Y	Cavity-filling	0.3[a]
H1058W	Cavity-filling	<0.5[b]
H1058F	Cavity-filling	0[b]
H1058Y	Cavity-filling	0.3[a]
A1078C, V1133C	Disulfide	<0.5[b]
A1080C, I1132C	Disulfide	<0.5[b]
I1081C, N1135C	Disulfide	0.3[a]
H1088Y	Cavity-filling	1.6[a]
H1088W	Cavity-filling	0.6[a]
F1103C, P1112C	Disulfide	0.15[a]
V1104I	Cavity-filling	0.7[a]
T1116C, Y1138C	Disulfide	0[b]
T1117C, D1139C	Disulfide	1.0[a]
D1118F	Charge removal, pi-pi stacking	0.5[b]
I1130Y	Hydrogen bond	0[b]
L1141F	Cavity-filling	0.8[a]
ΔHR2 (Δ1161-1208)	Remove flexible region	2.5[a]

[a]Quantified using the area under the curve of the size-exclusion trimer peak
[b]Quantified using SDS-PAGE band intensity

Table S2. Expression summary of Combo variants.

Combo #	Substitutions	Strategy	Fold change in expression relative to S-2P
Combo1	A903C, Q913C, Q965C, S1003C	Disulfide+Disulfide	2.2
Combo2	S884C, A893C, A903C, Q913C	Disulfide+Disulfide	0.8
Combo3	T791C, A879C, A903C, Q913C	Disulfide+Disulfide	0.5
Combo4	G799C, A924C, A903C, Q913C	Disulfide+Disulfide	0.5
Combo8	T791C, A879C, S884C, A893C	Disulfide+Disulfide	0.5
Combo9	G799C, A924C, S884C, A893C	Disulfide+Disulfide	0.4
Combo11	A892P, A899P	Proline+Proline	1.9
Combo12	A892P, T912P	Proline+Proline	2.7
Combo14	A892P, A942P	Proline+Proline	6.2
Combo16	A899P, A942P	Proline+Proline	5.1
Combo19	L938F, A892P	Cavity-filling+Proline	3.0
Combo20	L938F, A899P	Cavity-filling+Proline	3.0
Combo21	F817P, L938F	Proline+Proline	3.9
Combo22	L938F, A942P	Cavity-filling+Proline	6.0
Combo23	S884C, A893C, L938F	Disulfide+Cavity-filling	2.9
Combo24	T791C, A879C, L938F	Disulfide+Cavity-filling	2.2
Combo26	L938F, A903C, Q913C	Cavity-filling+Disulfide	2.0
Combo40	F817P, S884C, A893C	Proline+Disulfide	2.0
Combo42	T791C, A879C, F817P	Disulfide+Proline	1.4
Combo45	A892P, A899P, A942P	3X Proline	6.2
Combo46	F817P, A892P, A899P	3X Proline	3.8
Combo47	F817P, A892P, A899P, A942P	4X Proline	9.8

Table S3. Cryo-EM data collection and refinement statistics.

EM data collection and reconstruction statistics

Protein	SARS-CoV-2 S HexaPro One RBD Up	SARS-CoV-2 S HexaPro Two RBDs Up
EMDB	EMD-22221	EMD-22222
Microscope	FEI Titan Krios	FEI Titan Krios
Voltage (kV)	300	300
Detector	Gatan K3	Gatan K3
Magnification	81,000	81,000
Pixel size (Å/pix)	1.08	1.08
Frames per exposure	40	40
Exposure (e$^-$/Å^2)	45	45
Defocus range (μm)	0.8-2.3	0.8-2.3
Micrographs collected	3,511	3,511
Particles extracted/final	695,490 / 85,675	695,490 / 90,274
Symmetry imposed	n/a (C1)	n/a (C1)
Masked resolution at 0.143 FSC (Å)	3.21	3.20

Model refinement and validation statistics

PDB ID	6XKL
Composition	
Amino acids	2,920
Glycans	50
RMSD bonds (Å)	0.008
RMSD angles (º)	1.01
Mean B-factors	
Amino acids	37.9
Glycans	55
Ramachandran	
Favored (%)	95.8
Allowed (%)	4.1
Outliers (%)	0.1
Rotamer outliers (%)	3.6
Clash score	6.39
C-beta outliers (%)	0.0
CaBLAM outliers (%)	2.57
MolProbity score	2.07
EMRinger score	3.00

References

1. J. F. W. Chan, S. Yuan, K. H. Kok, K. K. W. To, H. Chu, J. Yang, F. Xing, J. Liu, C. C. Y. Yip, R. W. S. Poon, H. W. Tsoi, S. K. F. Lo, K. H. Chan, V. K. M. Poon, W. M. Chan, J. D. Ip, J. P. Cai, V. C. C. Cheng, H. Chen, C. K. M. Hui, K. Y. Yuen, A familial cluster of pneumonia associated with the 2019 novel coronavirus indicating person-to-person transmission: A study of a family cluster. *Lancet* **395**, 514–523 (2020). [doi:10.1016/S0140-6736(20)30154-9](doi:10.1016/S0140-6736(20)30154-9) Medline

2. C. Huang, Y. Wang, X. Li, L. Ren, J. Zhao, Y. Hu, L. Zhang, G. Fan, J. Xu, X. Gu, Z. Cheng, T. Yu, J. Xia, Y. Wei, W. Wu, X. Xie, W. Yin, H. Li, M. Liu, Y. Xiao, H. Gao, L. Guo, J. Xie, G. Wang, R. Jiang, Z. Gao, Q. Jin, J. Wang, B. Cao, Clinical features of patients infected with 2019 novel coronavirus in Wuhan, China. *Lancet* **395**, 497–506 (2020). [doi:10.1016/S0140-6736(20)30183-5](doi:10.1016/S0140-6736(20)30183-5) Medline

3. F. Li, Structure, Function, and Evolution of Coronavirus Spike Proteins. *Annu. Rev. Virol.* **3**, 237–261 (2016). doi:10.1146/annurev-virology-110615-042301 Medline

4. M. Hoffmann, H. Kleine-Weber, S. Schroeder, N. Krüger, T. Herrler, S. Erichsen, T. S. Schiergens, G. Herrler, N. H. Wu, A. Nitsche, M. A. Müller, C. Drosten, S. Pöhlmann, SARS-CoV-2 Cell Entry Depends on ACE2 and TMPRSS2 and Is Blocked by a Clinically Proven Protease Inhibitor. *Cell* **181**, 271–280.e8 (2020). doi:10.1016/j.cell.2020.02.052 Medline

5. Y. Wan, J. Shang, R. Graham, R. S. Baric, F. Li, Receptor Recognition by the Novel Coronavirus from Wuhan: An Analysis Based on Decade-Long Structural Studies of SARS Coronavirus. *J. Virol.* **94**, e00127 (2020). [doi:10.1128/JVI.00127-20](doi:10.1128/JVI.00127-20) Medline

6. P. Zhou, X. L. Yang, X. G. Wang, B. Hu, L. Zhang, W. Zhang, H. R. Si, Y. Zhu, B. Li, C. L. Huang, H. D. Chen, J. Chen, Y. Luo, H. Guo, R. D. Jiang, M. Q. Liu, Y. Chen, X. R. Shen, X. Wang, X. S. Zheng, K. Zhao, Q. J. Chen, F. Deng, L. L. Liu, B. Yan, F. X. Zhan, Y. Y. Wang, G. F. Xiao, Z. L. Shi, A pneumonia outbreak associated with a new coronavirus of probable bat origin. *Nature* **579**, 270–273 (2020). [doi:10.1038/s41586-020-2012-7](doi:10.1038/s41586-020-2012-7) Medline

7. B. J. Bosch, R. van der Zee, C. A. de Haan, J. M. Rottier, The coronavirus spike protein is a class I virus fusion protein: Structural and functional characterization of the fusion core complex. *J. Virol.* **77**, 8801–8811 (2003). [doi:10.1128/JVI.77.16.8801-8811.2003](doi:10.1128/JVI.77.16.8801-8811.2003) Medline

8. A. C. Walls, M. A. Tortorici, J. Snijder, X. Xiong, B. J. Bosch, F. A. Rey, D. Veesler, Tectonic conformational changes of a coronavirus spike glycoprotein promote membrane fusion. *Proc. Natl. Acad. Sci. U.S.A.* **114**, 11157–11162 (2017). doi:10.1073/pnas.1708727114 Medline

9. U. J. Buchholz, A. Bukreyev, L. Yang, E. W. Lamirande, B. R. Murphy, K. Subbarao, P. L. Collins, Contributions of the structural proteins of severe acute respiratory syndrome coronavirus to protective immunity. *Proc. Natl. Acad. Sci. U.S.A.* **101**, 9804–9809 (2004). doi:10.1073/pnas.0403492101 Medline

10. H. Hofmann, K. Hattermann, A. Marzi, T. Gramberg, M. Geier, M. Krumbiegel, S. Kuate, K. Überla, M. Niedrig, S. Pöhlmann, S protein of severe acute respiratory syndrome-associated coronavirus mediates entry into hepatoma cell lines and is targeted by neutralizing antibodies in infected patients. *J. Virol.* **78**, 6134–6142 (2004). [doi:10.1128/JVI.78.12.6134-6142.2004](doi:10.1128/JVI.78.12.6134-6142.2004) Medline

11. J. Pallesen, N. Wang, K. S. Corbett, D. Wrapp, R. N. Kirchdoerfer, H. L. Turner, C. A. Cottrell, M. M. Becker, L. Wang, W. Shi, W.-P. Kong, E. L. Andres, A. N. Kettenbach, M. R. Denison, J. D. Chappell, B. S. Graham, A. B. Ward, J. S. McLellan, Immunogenicity and structures of a rationally designed prefusion MERS-CoV spike antigen. *Proc. Natl. Acad. Sci. U.S.A.* **114**, E7348–E7357 (2017). doi:10.1073/pnas.1707304114 Medline

12. R. W. Sanders, R. Derking, A. Cupo, J.-P. Julien, A. Yasmeen, N. de Val, H. J. Kim, C. Blattner, A. T. de la Peña, J. Korzun, M. Golabek, K. de Los Reyes, T. J. Ketas, M. J. van Gils, C. R. King, I. A. Wilson, A. B. Ward, P. J. Klasse, J. P. Moore, A next-generation cleaved, soluble HIV-1 Env trimer, BG505 SOSIP.664 gp140, expresses multiple epitopes for broadly neutralizing but not non-neutralizing antibodies. *PLOS Pathog.* **9**, e1003618 (2013). doi:10.1371/journal.ppat.1003618 Medline

13. M. C. Crank, T. J. Ruckwardt, M. Chen, K. M. Morabito, E. Phung, P. J. Costner, L. A. Holman, S. P. Hickman, N. M. Berkowitz, I. J. Gordon, G. V. Yamshchikov, M. R. Gaudinski, A. Kumar, L. A. Chang, S. M. Moin, J. P. Hill, A. T. DiPiazza, R. M. Schwartz, L. Kueltzo, J. W. Cooper, P. Chen, J. A. Stein, K. Carlton, J. G. Gall, M. C. Nason, P. D. Kwong, G. L. Chen, J. R. Mascola, J. S. McLellan, J. E. Ledgerwood, B. S. Graham, VRC 317 Study Team, A proof of concept for structure-based vaccine design targeting RSV in humans. *Science* **365**, 505–509 (2019). doi:10.1126/science.aav9033 Medline

14. Y. J. Park, A. C. Walls, Z. Wang, M. M. Sauer, W. Li, M. A. Tortorici, B. J. Bosch, F. DiMaio, D. Veesler, Structures of MERS-CoV spike glycoprotein in complex with sialoside attachment receptors. *Nat. Struct. Mol. Biol.* **26**, 1151–1157 (2019). [doi:10.1038/s41594-019-0334-7](doi:10.1038/s41594-019-0334-7) Medline

15. Z. Li, A. C. A. Tomlinson, A. H. M. Wong, D. Zhou, M. Desforges, P. J. Talbot, S. Benlekbir, J. L. Rubinstein, J. M. Rini, The human coronavirus HCoV-229E S-protein structure and receptor binding. *eLife* **8**, e51230 (2019). doi:10.7554/eLife.51230 Medline

16. N. Wang, O. Rosen, L. Wang, H. L. Turner, L. J. Stevens, K. S. Corbett, C. A. Bowman, J. Pallesen, W. Shi, Y. Zhang, K. Leung, R. N. Kirchdoerfer, M. M. Becker, M. R. Denison,

J. D. Chappell, A. B. Ward, B. S. Graham, J. S. McLellan, Structural Definition of a Neutralization-Sensitive Epitope on the MERS-CoV S1-NTD. *Cell Rep.* **28**, 3395–3405.e6 (2019). doi:10.1016/j.celrep.2019.08.052 Medline

17. A. C. Walls, X. Xiong, Y.-J. Park, M. A. Tortorici, J. Snijder, J. Quispe, E. Cameroni, R. Gopal, M. Dai, A. Lanzavecchia, M. Zambon, F. A. Rey, D. Corti, D. Veesler, Unexpected Receptor Functional Mimicry Elucidates Activation of Coronavirus Fusion. *Cell* **176**, 1026–1039.e15 (2019). doi:10.1016/j.cell.2018.12.028 Medline

18. D. Wrapp, N. Wang, K. S. Corbett, J. A. Goldsmith, C. L. Hsieh, O. Abiona, B. S. Graham, J. S. McLellan, Cryo-EM structure of the 2019-nCoV spike in the prefusion conformation. *Science* **367**, 1260–1263 (2020). doi:10.1126/science.abb2507 Medline

19. A. C. Walls, Y. J. Park, M. A. Tortorici, A. Wall, A. T. McGuire, D. Veesler, Structure, Function, and Antigenicity of the SARS-CoV-2 Spike Glycoprotein. *Cell* **181**, 281–292.e6 (2020). doi:10.1016/j.cell.2020.02.058 Medline

20. J. S. McLellan, M. Chen, M. G. Joyce, M. Sastry, G. B. E. Stewart-Jones, Y. Yang, B. Zhang, L. Chen, S. Srivatsan, A. Zheng, T. Zhou, K. W. Graepel, A. Kumar, S. Moin, J. C. Boyington, G.-Y. Chuang, C. Soto, U. Baxa, A. Q. Bakker, H. Spits, T. Beaumont, Z. Zheng, N. Xia, S.-Y. Ko, J.-P. Todd, S. Rao, B. S. Graham, P. D. Kwong, Structure-based design of a fusion glycoprotein vaccine for respiratory syncytial virus. *Science* **342**, 592–598 (2013). doi:10.1126/science.1243283 Medline

21. L. Rutten, Y.-T. Lai, S. Blokland, D. Truan, I. J. M. Bisschop, N. M. Strokappe, A. Koornneef, D. van Manen, G.-Y. Chuang, S. K. Farney, H. Schuitemaker, P. D. Kwong, J. P. M. Langedijk, A Universal Approach to Optimize the Folding and Stability of Prefusion-Closed HIV-1 Envelope Trimers. *Cell Rep.* **23**, 584–595 (2018). doi:10.1016/j.celrep.2018.03.061 Medline

22. A. Krarup, D. Truan, P. Furmanova-Hollenstein, L. Bogaert, P. Bouchier, I. J. M. Bisschop, M. N. Widjojoatmodjo, R. Zahn, H. Schuitemaker, J. S. McLellan, J. P. M. Langedijk, A highly stable prefusion RSV F vaccine derived from structural analysis of the fusion mechanism. *Nat. Commun.* **6**, 8143 (2015). doi:10.1038/ncomms9143 Medline

23. L. Rutten, M. S. A. Gilman, S. Blokland, J. Juraszek, J. S. McLellan, J. P. M. Langedijk, Structure-Based Design of Prefusion-Stabilized Filovirus Glycoprotein Trimers. *Cell Rep.* **30**, 4540–4550.e3 (2020). doi:10.1016/j.celrep.2020.03.025 Medline

24. M. B. Battles, V. Más, E. Olmedillas, O. Cano, M. Vázquez, L. Rodríguez, J. A. Melero, J. S. McLellan, Structure and immunogenicity of pre-fusion-stabilized human metapneumovirus F glycoprotein. *Nat. Commun.* **8**, 1528 (2017). [doi:10.1038/s41467-017-01708-9](doi:10.1038/s41467-017-01708-9) Medline

25. H. Qiao, S. L. Pelletier, L. Hoffman, J. Hacker, R. T. Armstrong, J. M. White, Specific single or double proline substitutions in the "spring-loaded" coiled-coil region of the influenza

hemagglutinin impair or abolish membrane fusion activity. *J. Cell Biol.* **141**, 1335–1347 (1998). [doi:10.1083/jcb.141.6.1335](doi:10.1083/jcb.141.6.1335) Medline

26. K. M. Hastie, M. A. Zandonatti, L. M. Kleinfelter, M. L. Heinrich, M. M. Rowland, K. Chandran, L. M. Branco, J. E. Robinson, R. F. Garry, E. O. Saphire, Structural basis for antibody-mediated neutralization of Lassa virus. *Science* **356**, 923–928 (2017). doi:10.1126/science.aam7260 Medline

27. M. Yuan, N. C. Wu, X. Zhu, C. D. Lee, R. T. Y. So, H. Lv, C. K. P. Mok, I. A. Wilson, A highly conserved cryptic epitope in the receptor binding domains of SARS-CoV-2 and SARS-CoV. *Science* **368**, 630–633 (2020). doi:10.1126/science.abb7269 Medline

28. D. Tegunov, P. Cramer, Real-time cryo-electron microscopy data preprocessing with Warp. *Nat. Methods* **16**, 1146–1152 (2019). [doi:10.1038/s41592-019-0580-y](doi:10.1038/s41592-019-0580-y) Medline

29. A. Punjani, J. L. Rubinstein, D. J. Fleet, M. A. Brubaker, cryoSPARC: Algorithms for rapid unsupervised cryo-EM structure determination. *Nat. Methods* **14**, 290–296 (2017). doi:10.1038/nmeth.4169 Medline

30. E. Ramírez-Aportela, J. L. Vilas, A. Glukhova, R. Melero, P. Conesa, M. Martínez, D. Maluenda, J. Mota, A. Jiménez, J. Vargas, R. Marabini, P. M. Sexton, J. M. Carazo, C. O. S. Sorzano, Automatic local resolution-based sharpening of cryo-EM maps. *Bioinformatics* **36**, 765–772 (2020). Medline

31. P. Emsley, B. Lohkamp, W. G. Scott, K. Cowtan, Features and development of Coot. *Acta Crystallogr. D* **66**, 486–501 (2010). [doi:10.1107/S0907444910007493](doi:10.1107/S0907444910007493) Medline

32. D. Liebschner, P. V. Afonine, M. L. Baker, G. Bunkóczi, V. B. Chen, T. I. Croll, B. Hintze, L. W. Hung, S. Jain, A. J. McCoy, N. W. Moriarty, R. D. Oeffner, B. K. Poon, M. G. Prisant, R. J. Read, J. S. Richardson, D. C. Richardson, M. D. Sammito, O. V. Sobolev, D. H. Stockwell, T. C. Terwilliger, A. G. Urzhumtsev, L. L. Videau, C. J. Williams, P. D. Adams, Macromolecular structure determination using X-rays, neutrons and electrons: Recent developments in Phenix. *Acta Crystallogr. D* **75**, 861–877 (2019). [doi:10.1107/S2059798319011471](doi:10.1107/S2059798319011471) Medline

33. T. I. Croll, ISOLDE: A physically realistic environment for model building into low-resolution electron-density maps. *Acta Crystallogr. D* **74**, 519–530 (2018). [doi:10.1107/S2059798318002425](doi:10.1107/S2059798318002425) Medline